Synthesis of Biomass Combustion Fly Ash Derived Zeolites for CO_2 Adsorption: Optimisation of Hydrothermal Synthetic Pathway

Ben Petrovic, Mikhail Gorbounov, Salman Masoudi Soltani

Department of Chemical Engineering, Brunel University London, Uxbridge UB8 3PH, United Kingdom

Corresponding author's telephone: +44-(0)1895265884

Corresponding author's email: Salman.MasoudiSoltani@brunel.ac.uk

Abstract

Industrial biomass combustion fly ash has been investigated as a precursor for zeolites with a view to evaluate the potential for adsorption of CO_2. The synthesis methodology has been optimised *via* Design of Experiment by employing a Taguchi L9 array. Three variables were identified as statistically significant, the crystallisation temperature, crystallisation time and the liquid to solid ratio. Analysis of the main effects revealed an optimum set of conditions which produced a sample with the highest adsorption capacity of those prepared, 1.84 $mmolg^{-1}$ at 50 °C. This was a result of the conversion of the as-received fly ash into type A (LTA) and type X (FAU) zeolites after alkaline fusion with NaOH and hydrothermal treatment. The enthalpy of adsorption was estimated at -40.2$kJmol^{-1}$ and was shown to be dependent on surface coverage; the isosteric enthalpy of adsorption at zero coverage was -86 $kJmol^{-1}$. The working capacity of the adsorbent was maintained at 85% of the first adsorption uptake after a total of 40 cycles in a simulated temperature swing adsorption process (50 °C/150 °C adsorption/desorption). The equilibrium and kinetic CO_2 adsorption isotherms are presented and modelled through non-linear regression to reveal the adsorption mechanisms demonstrated by the fly ash-derived zeolites. Significant heterogeneity exists within the multi-phase zeolite which presents both micro and mesoporosity. The developed adsorbent presents a feasible route to valorisation of biomass combustion fly ash with good potential for application in the separation of CO_2.

Keywords: Carbon Capture, Adsorption, Biomass Combustion Ash, Zeolite

Table of Contents

Nomenclature

Acronyms	
ANOVA	Analysis of Variance
BET	Brunauer - Emmet - Teller
BFA/FA	Biomass Combustion Fly Ash/Fly Ash
BJH	Barret-Joyner-Halenda
CBU	Composite/Secondary Building Units
CCS	Carbon Capture and Storage
CCUS	Carbon Capture, Utilisation & Storage
CDR	Carbon Dioxide Removal
D4R	Double 4-rings
D6R	Double 6-rings
DAC	Direct Air Capture
DoE	Design of Experiment
EDS	Energy Dispersive X-Ray Spectroscopy
FAU	Faujasite
IPCC	Intergovernmental Panel on Climate Change
IPD	Weber & Morris Intraparticle Diffusion Model
IUPAC	International Union of Pure and Applied Chemistry
LTA	Linde Type A
MR	Member Ring
PFO	Pseudo First Order
PSO	Pseudo Second Order
RMSE	Root Mean Squared Error
SEM	Scanning Electron Microscopy
SESAMI	Script to Estimate the Surface Area of Materials from their Isotherms
SNR	Signal to Noise Ratio
TGA	Thermogravimetric Analysis
XRD	X-ray Diffraction
Symbols	
S_{BET}	Surface Area (BET)
L/S	Liquid to Solid Ratio
T_{cry}	Crystallisation Temperature
t_{cry}	Crystallisation Time
$NaOH/FA$	Sodium Hydroxide to Fly Ash Ratio
P	Pressure
P_0	Saturation Pressure
$Å$	Angstrom
R_2	Coefficient of Determination
$adj\text{-}\ R_2$	Adjusted R^2
q_{max}	Predicted Saturation Capacity
K_T	Toth Affinity Parameter
n_T	Toth Constant
q_t	Adsorbed Amount at Time t
k_{IPD}	Intraparticle Diffusion Model Rate Constant

1. Introduction

The first UK CCUS projects are due to come online in 2027 with further expansion anticipated throughout the decade. The intention for these clusters is to remove and store 20 – 30 Mt CO_2 per year by 2030 [1]. These efforts however, may not be sufficient to avoid the 1.5 °C warming by 2050 [2,3]. The Intergovernmental Panel on Climate Change (IPCC) anticipates that current trends will lead to a breach of the 1.5 °C limit in the first half of the 2030s [4]. As a complement to the decarbonisation of power and industry, net Carbon Dioxide Removal (CDR) is gaining increasing attention, with most efforts aligned to either Direct Air Capture (DAC) [5] or Bioenergy with CCS (BECCS) [6]. BECCS can create a net-negative flow of CO_2 from the atmosphere into storage since CO_2 is sequestered in the biomass during growth; if this same CO_2 is then captured and stored at the end-use of the biomass (*e.g.* as a fuel in combustion) there is net-removal of CO_2 from the wider environment. In the UK, during their sixth carbon budget, the Committee on Climate Change estimated that BECCS could facilitate CO_2 removal of up to 22 Mt CO_2 per year by 2035 and up to 53 Mt CO_2 per year by 2050 [7,8]. In 2022, biomass provided 11 % of the UK's 135 TWh of renewable generation making it the 2nd largest renewable energy source second only to the combined output of offshore and onshore wind power [9,10]. The largest power station in the UK, Drax power station, Selby runs exclusively on biomass (BE) and has ambitions to become carbon negative (BECCS) by 2030 [11].

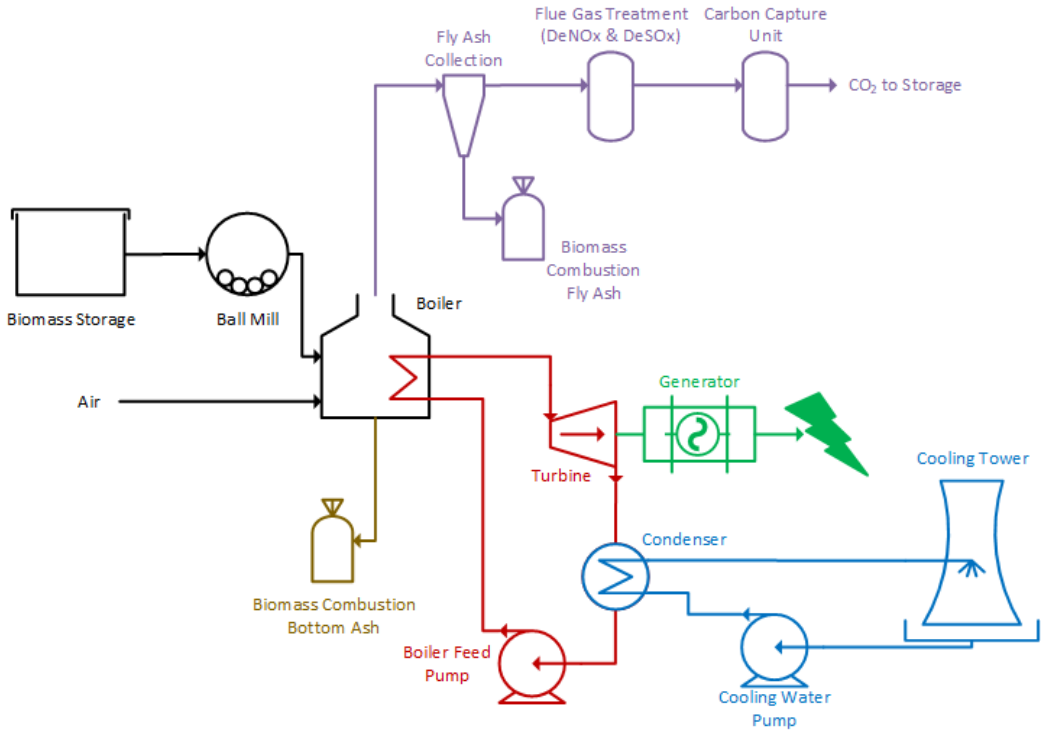

Figure 1: Schematic diagram of a thermal biomass-fired power plant.

Production of heat and electricity is typically achieved through combustion processes (Figure 1) and the industrial by-products of solid biomass or fossil fuel combustion consists of bottom and fly ashes. The former is dry or melt discharge and the latter from flue gas discharge systems, often electrostatic

precipitators or candle filters, or both. Raw biomass is a mixture of organic and inorganic matter, their ashes are generally embodied by a mixture of SiO_2, Al_2O_3, CaO, MgO, K_2O, Fe_2O_3, P_2O_5, and SO_3 [12]. There are however, significant variations in their compositions based on the biomass species used in the combustion process, growing conditions, harvest time/technique, transport and storage, method of processing and the combustion [13]. Biomass ashes present lower levels of toxic metals (vs coal) [14] and higher levels of alkali and alkaline earth elements [15]. This elevated alkali/alkaline earth metal renders them somewhat dissimilar to coal ashes and ultimately, owing to the range of variation, limits their secondary applications [16]. Considering the main constituents (silica and alumina) of these ash residues and the challenges associated with employing biomass-derived fly ash in typical secondary applications, these specific components could be recovered and employed in the synthesis of value-added products. Maximising the yield from such a waste, zeolites, a class of solid materials employed in adsorption and catalytic operations are extremely promising, a potential coup de grâce. Zeolite synthesis from waste residues is not a new research focus and has been of interest since the 1990s. There are however, limited studies pertaining to industrial-grade biomass combustion residues. Ash in the truest sense describes the residual solids after complete conversion of the solid precursor [17]. Despite this, most literature is inconsistent with this definition, and ash has often been referred to as any residue remaining after some physical or chemical conversion. The amount, chemical composition and size distribution of ash is highly dependent on the fuel and the form of the inorganic constituents as well as the configuration of the combustion system (temperatures, atmospheres), fuel preparation (*e.g.* grinding, washing) and boiler type [18]. The production of ash in a laboratory environment is inevitably unable to replicate both the temperature-profile and oxidising/reducing atmospheres within an industrial furnace. These factors have a significant effect on the physicochemical properties of the ash such as the development of particle structures, the fragmentation behaviour of char and ultimately the mechanism by which ash is formed [19].

The first CCS plants to come online will make use of absorption processes that require significant energy requirements for the regeneration of the working solvent [20]. An adsorption process operating *via* pressure or vacuum swing requires only a small pressure change to regenerate the adsorbent [21]. Two classes of materials alternative to zeolites are often investigated for CO_2 adsorption: carbonaceous adsorbents and metal-organic frameworks (MOFs). Carbonaceous materials in their non-functionalised form present good hydrophobicity but relatively weak interactions with CO_2 [22]. This weak interaction can lead to a low adsorption capacity and selectivity at low partial pressures. When tuning both the textural properties (pore size, volume, surface area) through activation or surface functionality through modification/doping, these can be improved, often quite significantly [23]. Doping with nitrogen, however, typically increases the enthalpy of adsorption (and selectivity of CO_2/N_2) but to the detriment of moisture sensitivity [24]. MOFs, arguably encompass a larger class of materials than that of zeolites and are characterised by extremely high specific surface areas and hence, comparable adsorption

capacities at elevated pressure [25,26]. In the context of post-combustion carbon capture, MOFs can be less suitable as CO_2 partial pressures are typically much lower (0.05 – 0.15 bar(a)) and the interaction between these materials and CO_2 is often lower than that exhibited by zeolites. Due to this, zeolites are often able to reach their maximum CO_2 uptake at low adsorption pressures. This phenomena is a result of the strong electrostatic interactions between CO_2 and the zeolite framework cations (Figure 2 (a) and (b) [27].

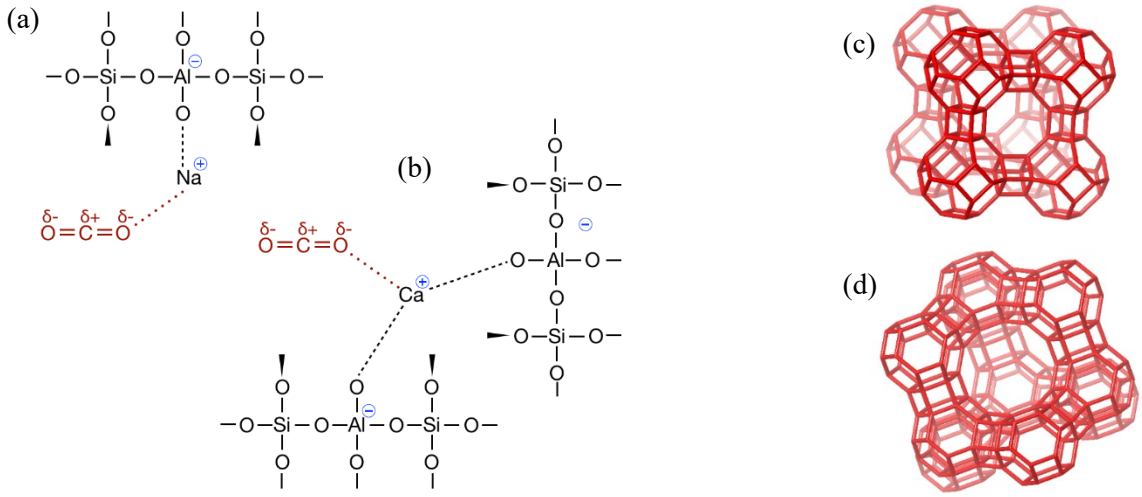

Figure 2: Interactions between CO_2 and monovalent (a) and divalent (b) cations in the zeolite framework; (c) Unit cell of Linde Type A (LTA); and (d) unit cell of Faujasite (FAU)[103].

The traditional hydrothermal scheme for the synthesis of crystalline zeolites involves mixing a source of both silica and alumina alongside a cation source in a basic medium. With the subsequent application of heat in a sealed autoclave [28], spontaneous nucleation and crystallisation processes are initiated [29]. In the context of gas separation processes, synthetic zeolites which possess Linde Type A (LTA) and Faujasite (FAU) structures are commonplace. These two unit cells (Figure 2 (c) and (d)) present the same connected cage topology and comprise similar CBUs with sodalite cages linked by double 4-rings (D4R) for the former and double 6-rings (D6R) for the latter [30]. The morphology of these, however, is significantly different, LTA structures present cubic arrangements, FAU hexaoctahedral [31]. As a source of both aluminium and silicon (and to some extent the cations), fly ashes, which present both crystalline and amorphous [32] aluminosilicate phases require pre-treatment to maximise availability of the primary building units. Fly ash zeolite synthesis pathways are diverse and the authors would direct the reader to a number of comprehensive reviews on the topic [12,14,33,34]. A common feature is the need to increase the solubility of the silicon and aluminium species in the fly ash. Fusion with an alkali such as NaOH is typical and results in soluble sodium aluminosilicates [12,35] which can be dispersed into an aqueous solution before aging and subsequent hydrothermal treatment [36].

Although there has been a steady increase in the number publications on the topic of “fly ash” and “zeolite” since the 1990’s, publications which feature “biomass fly ash” and “zeolite” are only present

from the late 2000's with significant increase in the last 10 years (Figure 3). In this work, the hydrothermal pathway for zeolite synthesis from biomass ash is optimised *via* Taguchi Design of Experiment. The fly ash precursor and optimum zeolite product is comprehensively characterised in respect of material properties. The optimum zeolite product is evaluated for its performance in CO_2 adsorption using thermogravimetric and volumetric equipment further supported by estimation of adsorption equilibria and kinetics.

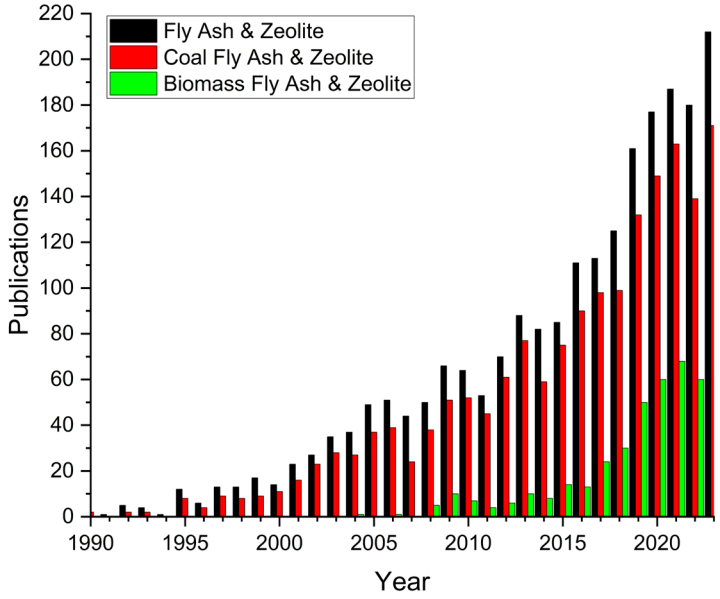

Figure 3: Publications indexed on SCOPUS by publication year.

2. Materials and Methodology

Biomass combustion fly ash (BFA) was sourced from Drax Power Station, Selby, UK, and is produced through combustion of imported white wood pellets. Sodium hydroxide was procured from Sigma Aldrich (≥ 97%) whilst the CO_2 (N2.8) and N_2 (N4.8) gases were sourced from BOC, UK. The alkaline fusion-assisted hydrothermal procedure was developed from previous works [30,37] and adjusted for each synthesis as per the experimental design. For each synthesis 5 g BFA was mixed with NaOH and ground manually in an unglazed alumina pestle and mortar for 5 minutes. Subsequently the mixture was placed into a nickel crucible and fused in a muffle furnace at 550 °C for 1 h (ramp rate of 5 °C·min^{-1} from ambient). The fused product was crushed and ground in a pestle and mortar before adding to deionised water in a PTFE liner. This mixture was then aged under mechanical/magnetic stirring at 500 RPM, 25 °C for 16 h. After insertion of the liner into a stainless-steel pressure vessel (Berghof DAB-3) it was then heated in an oven to a set temperature (ramp rate of 0.5 °C·min^{-1} from ambient). Upon completion the system was allowed to cool to around 40 °C before removing the liner and decanting and disposing of the supernatant. The solid product was separated and washed *via* vacuum filtration to a pH of 9. Finally, the product is dried overnight at 110 °C before grinding to a fine powder and weighing.

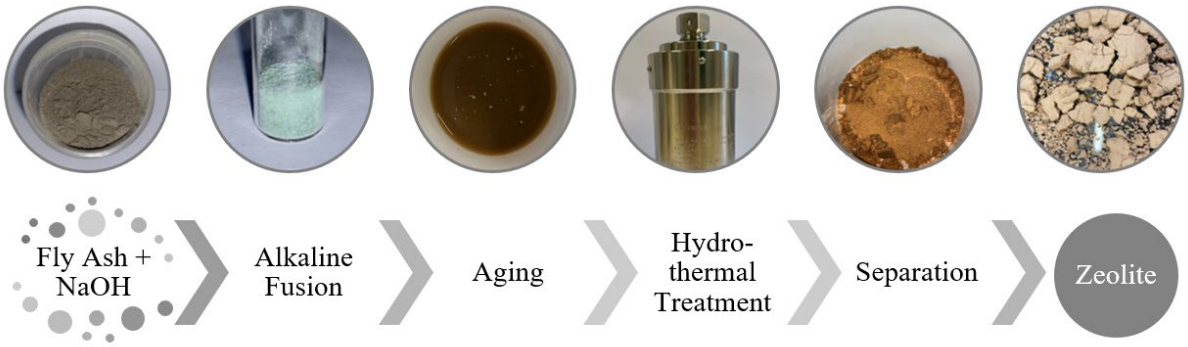

Figure 4: The procedure for synthesising fly-ash derived zeolites employed in this work.

2.1. Experimental Design – L9 Taguchi O.A.

The use of statistical techniques in the design and optimisation of experimental campaigns is of varied efficacy and is heavily dependent on the appropriate application of such tools including the selection of suitable factors and their levels [38]. A Taguchi L^9 design is employed in this work to study the effect of 4 factors on the CO_2 adsorption capacity of zeolitic adsorbents produced hydrothermally. The 4 factors and their 3 levels (+1, 0 and -1) are provided in Table 1. Selection of these factors is based on their key influence in the hydrothermal and alkaline-fusion hydrothermal synthesis procedures [12]. This work aims to identify an optimum BFA-derived zeolite with the least additional cost or complexity, control of factors aside from those directly influencing the synthesis methodology such as Si/Al ratio have not been considered as these become increasingly important when targeting a specific zeolite structure. The levels selected in this work were informed through previous works [30,37] which sought to reveal the experimental domain suitable for production of crystalline zeolitic products appropriate for CO_2 capture (*i.e.* FAU and LTA). The objective function for optimisation is the maximisation of equilibrium CO_2 adsorption capacity at 1 atm and 50 °C estimated gravimetrically *via* TGA. The temperature was selected to align with that of a thermal power plant after exhaust gas cleaning units. The two statistical tools employed in this work to analyse the L^9 Taguchi DoE are the signal-to-noise ratios (SNR) and Analysis of Variance (ANOVA) [39]. With regards to the former, of the three individual forms, the 'larger the better' SNR is used. The technique of ANOVA dissects variation into their respective sources and facilitates interpretation of the results with identification of those factors with statistical significance.

Table 1: Taguchi L9 O.A. exhibiting the 4 factors and respective levels studied in this work.

Run	NaOH/FA (w/w)	Crystallisation Time (h)	Crystallisation Temp (°C)	Liquid/Solid (w/w)	Sample Name
1	1.8	2	50	5	Z - 1.8/2/50/5
2	1.8	6	70	6	Z - 1.8/6/70/6
3	1.8	10	90	7	Z - 1.8/10/90/7

4	2	2	70	7	Z - 2/2/70/7
5	2	6	90	5	Z - 2/6/90/5
6	2	10	50	6	Z - 2/10/50/6
7	2.2	2	90	6	Z - 2.2/2/90/6
8	2.2	6	50	7	Z - 2.2/6/50/7
9	2.2	10	70	5	Z - 2.2/10/70/5

2.2. Material Characterisation

The as-received industrial-grade BFA and the optimum zeolite product have been characterised *via* Scanning Electron Microscopy (SEM) using a Zeiss LEO 1455VP instrument after gold-coating *via* the sputtering technique to minimise charging of the non-conductive samples during analysis. The elemental analysis of both the BFA and zeolite was evaluated through Energy Dispersive X-Ray Spectroscopy (EDS) using an Oxford INCAx-act system. The phases present in the BFA precursor and zeolite product were identified through X-Ray Diffraction (XRD) using a Bruker D8 diffractometer equipped with a copper tube and Lynxeye position sensitive detector in a 2theta range of 5 – 70 °, with a scan step size equal to 0.01°. The phases present within each product were identified using the Bruker Diffrac.EVA software package. The equilibrium CO_2 adsorption capacity of each sample was employed as the dependent variable for the optimisation. The equilibrium CO_2 adsorption capacity was measured using thermogravimetric analysis (TGA, Mettler Toledo TGA 2) under a stream of pure CO_2 at 50 °C after an initial degassing at 150 °C under pure N_2 for 2 h. The effect of temperature on the adsorption kinetics and equilibrium capacity has also been assessed *via* TGA at 25, 50 and 75 °C. The working capacity of the optimum zeolite has been evaluated at 50 °C by repeating the TGA programme for 40 adsorption/desorption cycles. Equilibrium adsorption isotherms have been generated *via* volumetric analyses (Micromeritics ASAP 2020) at 0, 10, 20, 25, and 40 °C between 0 and 1 bar(a). Nonlinear regression has been employed to fit models to both the kinetic and equilibrium data. The enthalpy of adsorption has been calculated *via* the Clausius Clapeyron equation with the equilibrium isotherms produced at 5 different temperatures. The porous surface area (S_{BET}) was obtained following the Brunauer – Emmett – Teller Method [40] using a Micromeritics 3Flex Analyser under pure N_2 at 77K after degassing at 350 °C for 12 h (10 °C·min^{-1}) with microporosity estimations *via* the t-plot method.

3. Results and Discussions

3.1. Taguchi Optimisation

The results from the synthesis campaign are presented in Table 2. The yields are calculated with reference to the initial mass of BFA (5 g) added prior to fusion with NaOH:

$$\frac{mass\ of\ product\ (g)}{mass\ of\ BFA\ (g)} \times 100 = Yield\ (\%)$$

The equilibrium uptakes (mmol·g^{-1}) were estimated *via* TGA using pure CO_2 at 1 bar(a) and 50°C after purging the samples under N_2 at 150 °C for 1 h. The results demonstrate that the products' uptakes are centred at either 0.6 and 1.6 mmol·g^{-1} which when considering the x-ray diffractograms (Figure 8) would suggest the former is indicative of amorphous aluminosilicates and the latter of crystalline zeolitic phases.

Table 2: Product yield (as percent of initial BFA weight) and equilibrium CO_2 adsorption capacity at 50 °C and 1 atm.

Sample	Yield (% of BFA converted)	Equilibrium Uptake @ 50°C (mmol·g^{-1})
Z - 1.8/2/50/5	70.75	0.65
Z - 1.8/6/70/6	75.31	0.61
Z - 1.8/10/90/7	80.86	1.51
Z - 2/2/70/7	71.44	0.56
Z - 2/6/90/5	71.47	1.67
Z - 2/10/50/6	73.53	0.56
Z - 2.2/2/90/6	71.35	0.59
Z - 2.2/6/50/7	72.34	0.49
Z - 2.2/10/70/5	72.92	1.70

Signal-to-noise ratios can be used for identification of the factor levels which minimise the variability in the response, in this case the objective is to maximise the equilibrium CO_2 adsorption capacity. The "larger the better" equation is adopted for calculation of the SNRs (EQ. 1). The SNRs are given in Table 3. The delta values represent the variation in the mean SNR values across the studied levels, and allow ranking of the factors' relative importance on the equilibrium CO_2 uptake when varied within the design space [39]. The analysis suggests a sequence that follows $L/S > T_{cry} > t_{cry} > NaOH/FA$.

$$\frac{S}{N} = -10 \cdot \log\left(\sum\left(\frac{1}{y^2}\right) / n\right) \qquad (EQ.\ 1)$$

Table 3: Response table for the signal to noise ratios.

Level	NaOH/FA Ratio	Crystallisation Time	Crystallisation Temperature	Liquid/Solid Ratio
1	-1.485	-4.454	-4.991	1.774
2	-1.873	-2.012	-1.574	-4.638
3	-2.057	1.041	1.15	-2.551
Delta	0.571	5.504	6.142	6.411
Rank	4	3	2	1

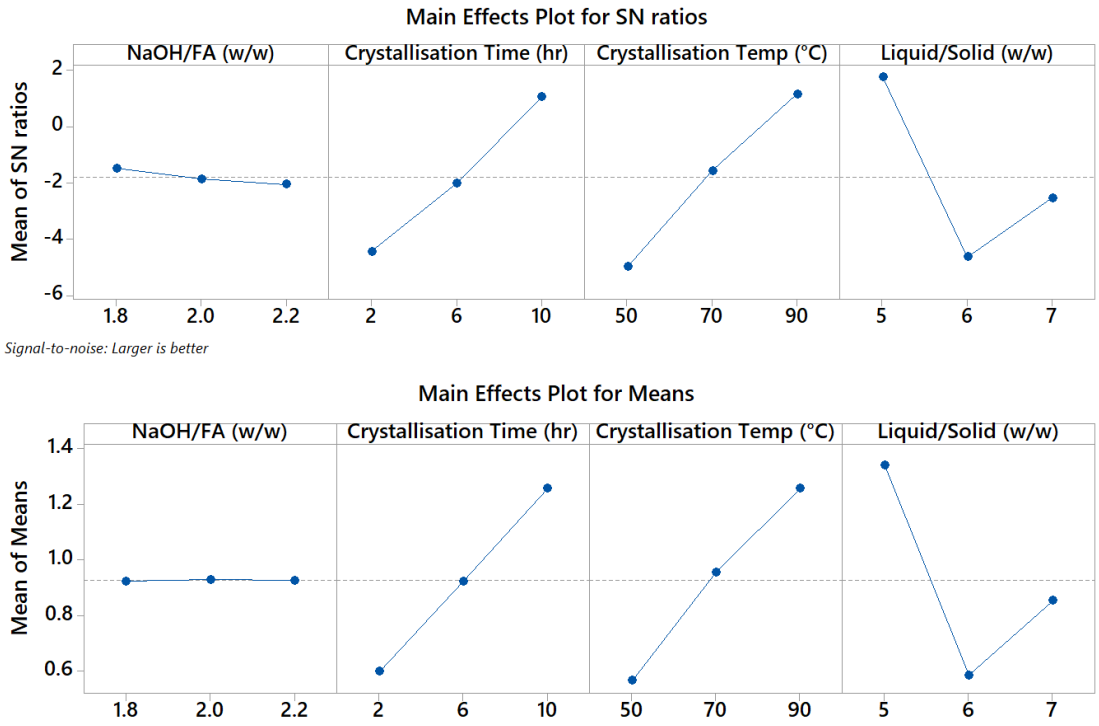

Figure 5: Main effects plot for the signal to noise ratios (top) and means (bottom).

The relative importance of each factor can also be observed graphically by plotting the main effects for the SNR ratios, provided in Figure 5. From this plot the *NaOH/FA* ratio has a minimal effect on the SNR ratio when compared to the other 3 factors. A factor which presents a large variation in the SNR between levels is a significant contributor to the dependent variable [41]; the SNR for *L/S*, T_{cry} and t_{cry} all exhibit strong main effects (gradient) in agreement with the delta values and subsequent ranking. The main effects have also been plotted for the means and are consistent with those for the SNRs except for the *NaOH/FA* ratio. Optimisation based on the main effects plots depends on the objective, either to minimise variability (SNR) or to simply maximise the response (mean). In this case and based on the main effects plot for the means, the optimum configuration of factors and levels would be: *NaOH/FA* ratio of 2.2, t_{cry} 10 hours, T_{cry} equal to 90 °C, and *L/S* equal to 5. One limitation with employing an L9 array to study four factors at three levels is that the model is overfit due to the presence of more fitting terms than observations (degrees of freedom) in the model [42]. Removal of some terms can facilitate the statistical analysis. In this case, based on the main effects plot, the *NaOH/FA* ratio term was removed. The ANOVA results for the remaining factors can be found in Table 4. Each of the factors present a p-value < 0.05 with significantly large F-values. The liquid to solid ratio (*L/S*) was identified as the most statistically significant factor. Within the employed synthesis, the L/S ratio determines both the relative alkalinity of the solution and the water content in the mixture. Both are key factors in the synthesis of zeolites [34] and will influence both the product structure type and crystallinity [43]. The percentage contribution of each factor to the equilibrium uptake is around 30 % for T_{cry} and t_{cry} rising to 39% for *L/S*; this agrees with the ranking identified in the SNR response table and main effects plot.

183 *Table 4: ANOVA results for the Taguchi L9 design.*

Factor	Percentage Contribution (%)	F-value	p-value	Order of Significance
Crystallisation Time (t_{cry})	29.49	5721.91	0.000	3
Crystallisation Temperature (T_{cry})	31.87	6183.58	0.000	2
Liquid/Solid Ratio (*L/S*)	38.63	7495.90	0.000	1

184 ### 3.1. Scanning Electron Microscopy and Energy Dispersive X-ray Spectroscopy

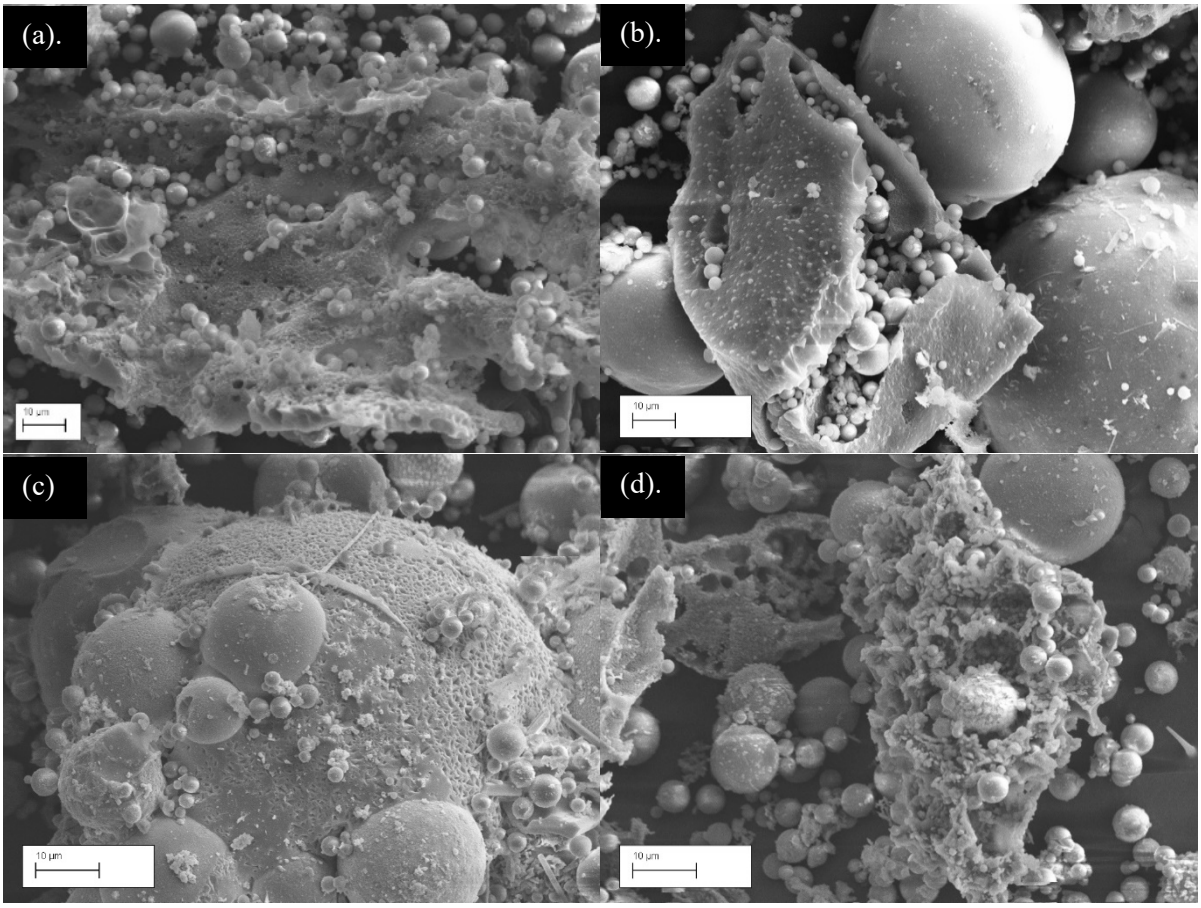

Figure 6: SEM images of the as-received biomass combustion fly ash: a) 20 kV, 500 pA; b) 20 kV, 300 pA; c) 10 kV, 50 pA; and d) 10 kV, 100 pA.

185 The BFA samples present predominately spherical particles of varying diameter with some of these in
186 large clusters. Typical ash particle shapes include molten spherical particles (Figure 6); cenospherical
187 particles with variable wall thickness typical of light ashes, which form during the sudden cooling post-
188 combustion [44]; plerospherical particles (hollow spheres filled with smaller ash particles) (not
189 observed); angular, sharp and unmolten particles (Figure 6 (a), (c) and (d)); loose, irregular shaped and
190 highly porous solids (Figure 6 (a), and (e)); and agglomerations of small ash particles (Figure 6 (a), (b)
191 and (d)) [18]. Biomass ashes present more varied morphologies than coal ashes and in the case of woody
192 biomass, loosely bound and irregularly shaped Ca-rich particles are frequently reported with sub-micron
193 salt particles (Figure 6 (c)) [18]. The abundance of calcium in wood-based fuels generally increases ash

melting temperatures by approximately 100 – 200 °C although this is dependent on the presence of other components within the ash [45]. Increased melt temperatures result in particles with more angular morphologies that haven't undergone melt/fusion, often composed of quartz or feldspars [17]. The elevated presence of inorganic constituents which during combustion vaporise is important during ash formation/deposition mechanisms as they lead to coagulation and agglomeration. The EDS revealed predominantly Si and Al in the BFA alongside Ca, K, Fe, Mg and Na. An average weight percentage has been calculated based on analysis of five sites on the BFA and are provided as part of Table 5. The measured diffractogram corroborates the elemental composition of the BFA. Crystalline quartz, mullite, hematite, portlandite and calcite were identified. Quartz can indeed remain unchanged during the combustion process and may maintain its sharp angular structure [46]; however, it can also form by conversion of kaolinite to mullite and amorphous quartz at around 900 °C [17]. Hematite is a high melting mineral and often forms from the decomposition of pyrite either through thermal decomposition and subsequent oxidation or direct oxidation [47]. Elements such as S and P (among others) and to some extent Ca, K, Mg and Na vaporise during the combustion reaction and then re-condense and form aerosols during cooling [18]. Sodium is well known to facilitate the formation of sodalite and other CBUs such as double-4 rings, whereas both Ca and K can present structure breaking effects [48]. The quantity of Al and Si highlights the potential suitability of this BFA as a zeolite-precursor. The inclusion of Ca within zeolites has also been reported as beneficial for CO_2 adsorption by enhancing the acidic-basic interactions [49]. Although not often considered a route for improvement of CO_2 adsorption, the presence of Fe as a charge compensating cation has been observed to improve the catalytic performance of FA-derived zeolites [50]. Both Fe and Ca oxides however, are known to hinder the zeolite nucleation rate [29] with the former a result of the lattice strains associated with the high Fe-O bond length (1.9 Å) and the latter due to the possible formation of calcium silicate hydrate over zeolitic phases [51,52].

Table 5: The EDS elemental analysis of the BFA and ZOPT averaged from five sites.

Element	Biomass Fly Ash Avg. Weight (%)	Zeolite (ZOPT) Avg. Weight (%)
Na	1.66	3.71
Mg	2.01	1.42
Al	9.15	10.05
Si	14.28	18.55
P	0.13	0.07
S	0.70	0.06
K	7.91	0.66
Ca	8.54	15.56
Fe	3.78	4.21

O	51.84	45.71

The morphology of the ZOPT sample can be observed in Figure 7. Examples of both cubic LTA and octahedral FAU are present confirming the findings of the XRD. The sample presents a relatively consistent individual crystal size of around 2 µm although the majority of these crystals are present in larger agglomerations of both crystals and what is assumed to be an amorphous mass. This amorphous mass will be the remaining aluminosilicates not consumed in the zeolite crystallisation process. None of the observed morphologies in the fly ash precursor remain further highlighting the efficacy of alkaline fusion to maximise the availability of soluble Si and Al containing species. As a complement to SEM and XRD, EDS can elucidate the presence of specific cations and their distributions within the crystalline frameworks and the amorphous constituent. Calcium was identified in most of the crystalline morphologies, and often at a higher weight percent than sodium. EDS analysis of five crystalline areas suggests the zeolitic phases present an average Si/Al weight ratio of approximately 1.85. Both iron and calcium are present in the sample at around 4 and 16 wt% so one could infer that there exists within ZOPT calcium exchanged type A and type X zeolites phases. EDS however, is semi-quantitative and fails to accurately measure low atomic number elements such as sodium due to their lower energy characteristic X-rays which are more difficult to reliably detect and often absorbed by the sample. A bulk analysis however, would be unable to accurately measure the composition of specific crystalline phases due to the presence of amorphous aluminosilicates.

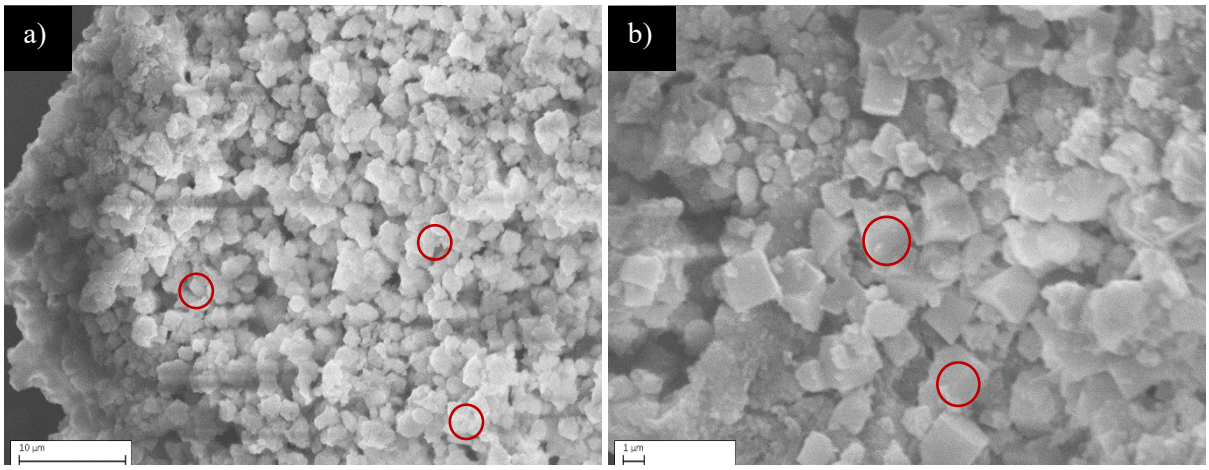

Figure 7: SEM images of ZOPT, a) 15kV and 40 pA and b)15kV and 40 pA. Red circles indicating site location for EDS analysis.

3.2. X-ray Diffraction

Powder X-ray diffraction is used to identify crystalline phases and of the 9 samples synthesised, 3 are distinctly crystalline: Z-1.8/10/90/7, Z-2/6/90/5 and Z-2.2/10/70/5. The remaining six samples all present a broad ridge centred at 30 ° 2theta which is indicative of amorphous aluminosilicates [53,54]. This ridge can also be seen in the crystalline phases indicating a non-complete conversion of these amorphous components into crystalline frameworks [30]. Sample Z-2/6/90/5 presents peaks with the largest intensities relative to the other samples as well as a less well-defined amorphous region corroborating the findings of the DoE analysis which identified a region of high capacity at elevated

hydrothermal temperatures. The phases identified in each of the crystalline samples were LTA and FAU zeolites. Although these phases possess similar building blocks they do present distinct diffraction patterns with some overlap. The samples which exhibit the higher CO_2 adsorption capacities tend to possess diffractograms with greater intensities of peaks characteristic of FAU zeolites such as the peak at a 2θ value of approximately 6 ° corresponding to the lattice plane (111). The peak centred at a 2θ value of approximately 7 ° is characteristic of LTA zeolites (200) and not present in FAU diffractograms, with the greatest intensity shown for Z-2.2/10/70/5. Although inference of mass ratios (LTA/FAU) through analysis of the relative intensity of diffractogram peaks is of poor accuracy, the uptakes corroborate the notion that samples Z-2.2/10/70/5 and Z-2/6/90/5 may possess a larger proportion of FAU than Z-1.8/10/90/7. The diffractograms generated for the 3 crystalline samples and the optimum (ZOPT) are provided in Figure 8 alongside those of type X (PDF: 01-070-2168) and type A (PDF: 01-089-8015) zeolites. As shown, ZOPT presents a better-defined pattern with increased peak intensities over the 3 other samples suggesting the optimisation has improved the samples crystallinity. Both the LTA (200) and FAU (111) peaks are more pronounced with ZOPT suggesting the synthesis conditions are more favourable for zeolite crystallisation also evidenced by a less pronounced amorphous ridge. The inference is that more of the alkali fused BFA has been consumed during crystallisation, hence the increased peak intensities. Interestingly, no phases which existed in the BFA precursor are present in any of the produced samples, suggesting the alkali fusion step in the synthesis has successfully converted the BFA into soluble Al and Si containing species.

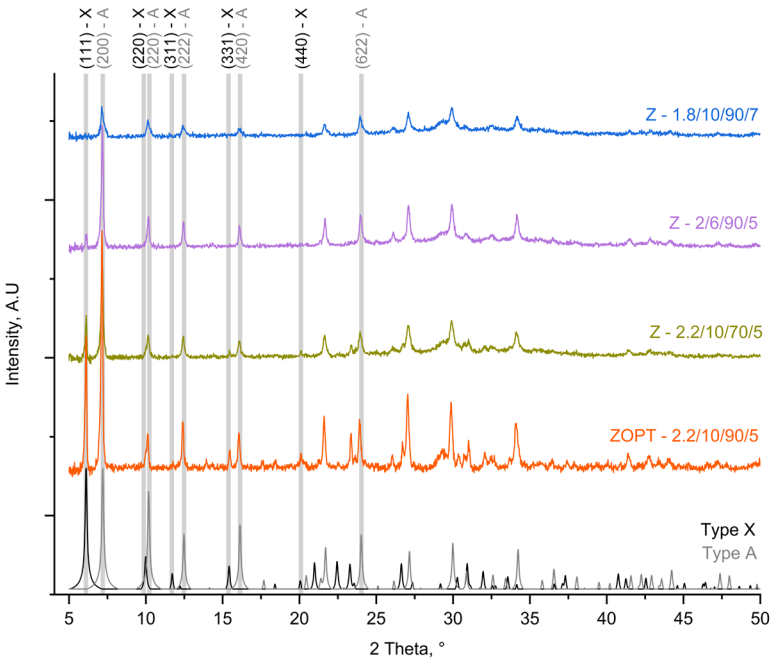

Figure 8: Powder x-ray diffractogram for crystalline zeolites produced in the L9 OA and the predicted optimum, ZOPT. Diffractograms provided for type X and type A zeolites adjacent to the y-axis.

3.3. Porosity and Surface Area Analysis

The BET surface area was estimated for ZOPT *via* isothermal N_2 adsorption and desorption at 77 K (Figure 9). The isotherm is of the type IV IUPAC classification, the initial knee indicative of primary micropore filling in pores of molecular dimensions at low relative pressures [55]. This is followed by the onset of capillary condensation in larger mesopores as P/P_0 increases [56]. A narrow hysteresis loop can be seen after $0.4 < P/P_0$; the adsorption branch being a composite of both type I and II isotherms suggests this to be an example of a H4 hysteresis [57]. This phenomena is typical for mixed micro-mesoporous materials [31] and can be a result of development of mesoporosity through aggregation of the individual zeolite crystals [58,59] and in this case can also include the contribution from the amorphous phase. Type IV isotherms often feature a plateau in adsorption when the relative pressure tends to 1 due to complete saturation/occupation of the adsorbent's mesopores *via* capillary condensation. This is not present in ZOPT resulting from the presence of macropores [60] causing an asymptotic increase in the adsorbed quantity at high relative pressures due to unrestricted multilayer formation. This phenomenon may result from significant structural defects in the crystalline phase or through aggregation [61]. The BET surface area has been calculated to be 321.60 $m^2 \cdot g^{-1}$, t-plot micropore area of 218.56 $m^2 \cdot g^{-1}$ with total (BJH) and t-plot micropore volumes of 0.23 $cm^3 \cdot g^{-1}$ and 0.09 $cm^3 \cdot g^{-1}$, respectively. The BET surface area has been estimated in the P/P_0 range of 0.016 and 0.059 to satisfy the criteria proposed by Rouquerol [62]; this deviates from the traditional range for BET surface area analysis (0.05 – 0.3) due to significant microporosity in the samples. The linear BET plot for N_2 at 77 K is provided as an inset to Figure 9.

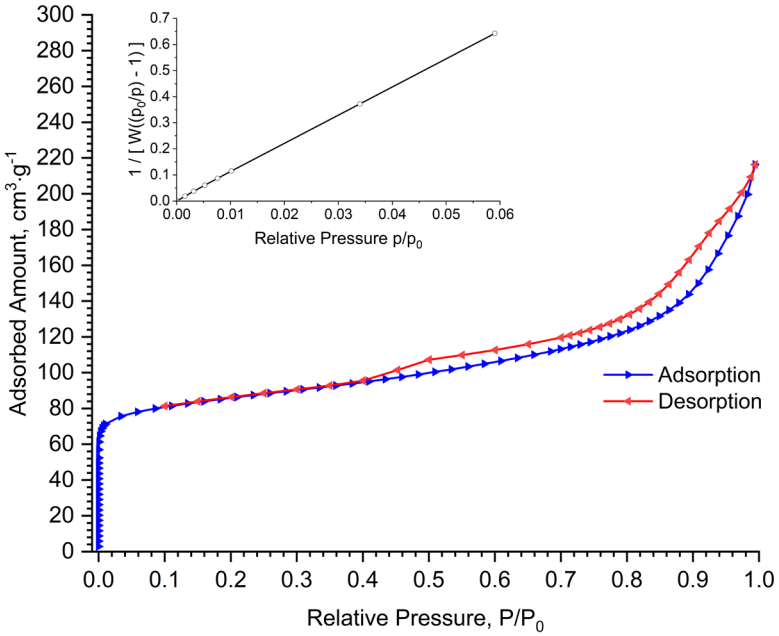

Figure 9: N_2 adsorption/desorption isotherm measured at 77 K (BET).

The surface area has also been estimated *via* analysis of the CO_2 adsorption isotherm at 0 °C. This method which is often used for characterising carbonaceous adsorbents overcomes the kinetic limitations associated with nitrogen adsorption at 77K [57]. The smaller kinetic diameter of CO_2 and the elevated temperature and pressure of analysis facilitate diffusion into narrow micropores inaccessible to N_2 at 77K. The high saturation pressure of CO_2 at these conditions however limits the maximum pore size that can be characterised to approximately 1 nm [63]. The calculations have been performed using SESAMI [64] with an adsorbed cross-sectional area of 21.8 Å and saturation pressure of 3.851408×10^6 Pa. Analysis of the linear region suggests a surface area of 432.30 m^2g^{-1}. This value represents a 111 m^2g^{-1} increase suggesting a large number of small micropores (<1 nm) in ZOPT which were not accessible to N_2 at 77K. Type A and X zeolites typically possess pores of size 4 and 7 Å, respectively which would explain the underestimation of surface area when using N_2. The analysis of ZOPT's pore size distribution has not been carried out due to the stronger quadrupole moment of CO_2 and the presence of polar groups within the zeolite making correlation of pore size and CO_2 pore filling pressure difficult [57].

3.4. CO_2 Adsorption

3.4.1. Screening

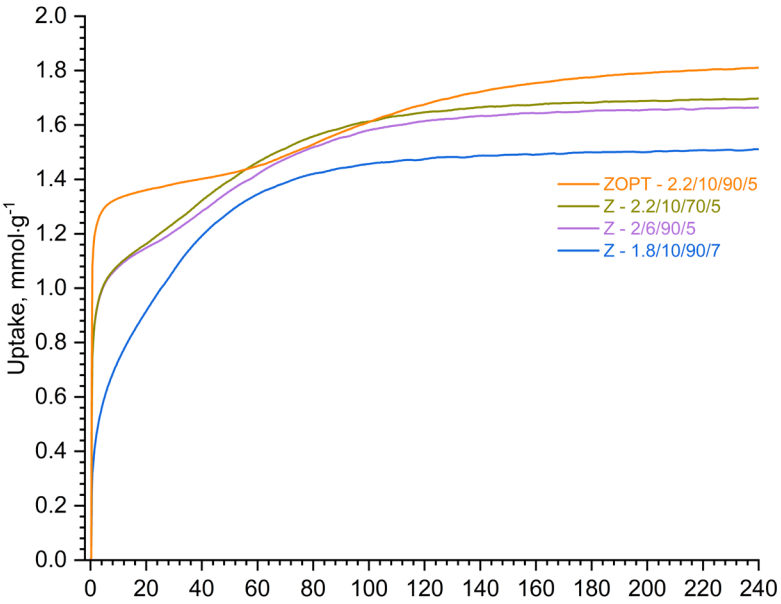

Figure 10: CO_2 uptake capacity measured via TGA under 1 atm at 50 °C.

The uptake capacity was used as the dependent variable for the Taguchi optimisation. Measured *via* TGA at 50 °C with pure CO_2 at 1 atm, the equilibrium uptakes are given in Table 2. The samples which lacked distinct crystalline phases all exhibit an equilibrium uptake of between 0.39 and 0.65 $mmolg^{-1}$. Although less than the crystalline counterpart, it is in agreement with the literature [65] and represents promising potential for geopolymer sorbents in the remit of CO_2 capture, especially if sourced from BFA. The three crystalline phases illustrate the efficacy of uniform-pore structure in gas adsorption

with equilibrium capacities between 1.50 to 1.70 $mmolg^{-1}$. The adsorption characteristics of Z-1.8/10/90/7 differ slightly from the two alternative crystalline samples, the initial phase of adsorption is slower, suggesting a crystalline phase or ratio of phases which is different to Z-2.2/10/70/5 and Z-2/6/90/5. These three samples have been synthesised at each of the NaOH/FA ratios, hence the associated statistical insignificance; None of the samples produced at a T_{cry} = 50 °C and L/S = 6 displayed high adsorption capacities, potentially as a result of failing to facilitate zeolitisation from the fused BFA. An extended measurement (4-hour adsorption time) was completed for ZOPT and the three crystalline samples produced according to the DoE (Figure 10). The sample with the highest equilibrium capacity is ZOPT at 1.84 $mmolg^{-1}$. This value represents an 8.2% increase over Z-2.2/10/70/5 and is comparable to the literature on other fly ash zeolites [31,66,67] and industrial biomass bottom ash derived adsorbents [16,42]. The only difference between the synthesis conditions of ZOPT and Z-2.2/10/70/5 is the elevated crystallisation temperature (90 vs 70 °C), suggesting that higher hydrothermal temperatures can preferentially produce FAU as observed in the XRD diffractograms (Figure 8). The CO_2 adsorption kinetics for FAU and LTA are markedly different, considering they both present the connected cage topologies [68]. The latter is considered a small pore zeolite, presenting a pore size of between 3 and 5 Å depending on the cation, whilst the former is above 7 Å [27]. The lower pore size is comparable to the kinetic diameter of CO_2 (3.3 Å) which can lead to a configurational diffusion regime with much lower gas diffusivity and consequently, slower adsorption kinetics. In a fixed bed configuration, slow diffusion of CO_2 into the zeolite pores would hinder mass transfer and result in a tendency for the CO_2 to flow through the bed rather than be adsorbed [27], reducing the breakthrough time and increasing the required bed height, cycle time and ultimately cost [69]. Type X zeolites (FAU) which present a 12-member ring, MR aperture (vs 8 for LTA) can facilitate diffusion in the Knudsen regime as the channel diameter is larger relative to the molecular diameter of CO_2. The transition from configurational diffusion to Knudsen occurs when the ratio of molecular to channel diameter, λ is below 0.6 (typically) however, for FAU this value is 0.45 [27,68]. The location and type of cations can also significantly affect the kinetics of CO_2 adsorption and is often more pronounced with type A than type X. The exchange of Na^+ with K^+ in LTA zeolites reduces the pore size of the zeolite from approximately 4 to 3 Å with site II being the preferential site (centre of the D8R) hindering diffusion by obstructing access to the alpha cage [70,71]. Exchange with a divalent atom such as Ca^{2+} reduces the occupation of site II and increases both the pore size (5 Å) and volume by improving accessibility to the alpha cage [72,73].

3.4.2. Equilibrium Adsorption

The equilibrium CO_2 adsorption isotherms have been measured volumetrically at 0, 10, 20, 25 and 40 °C in the total pressure range of 0 – 1 bar and are presented in Figure 11 . These isotherms are classical type I IUPAC isotherms featuring a sharp increase in the adsorbed quantity in the low pressure region [74]. This characteristic is influenced largely by the Si/Al ratio of zeolites as the aluminium content

dictates the required quantity of extra-framework cations [75] and hence any increase in Si/Al ratio would decrease the number of adsorption sites per unit mass of adsorbent [27]. Due to the lower electronegativity of Al (3+ vs 4+ for Si) there is a requirement for additional cation charge compensation which modifies the local electric field and hence increases the electric field gradient as Al content increases [76]. Structures such as LTA which typically possess an Si/Al ratio close to 1 and Type X (FAU) around 1.5, will exhibit good adsorption performance for CO_2. This also increases the co-adsorption of moisture [77] as the dipole moment of H_2O strongly competes with quadrupoles of CO_2 (despite being a non-polar molecule) for adsorption sites [78].

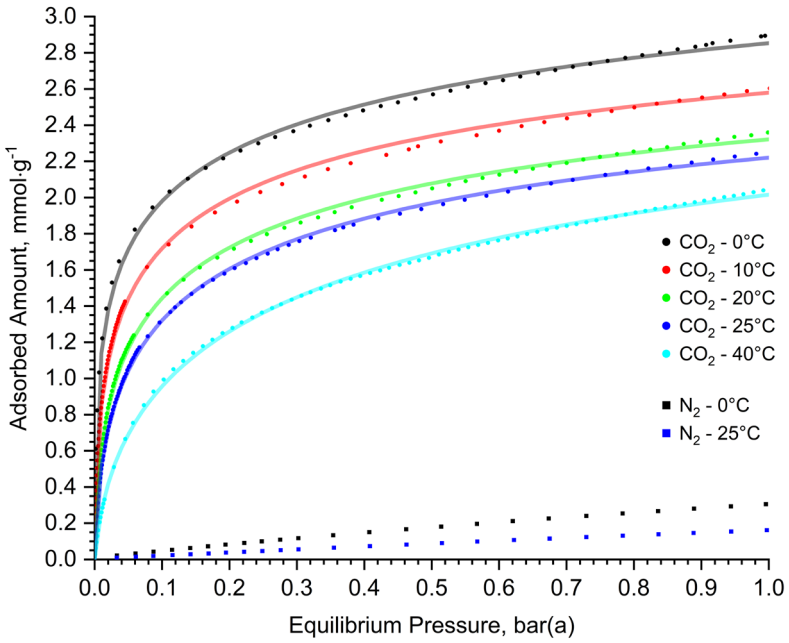

Figure 11: Measured equilibrium CO_2 adsorption isotherms (discrete data) and the Toth isotherm model (continuous data) fitted via non-linear regression analysis. Equilibrium N_2 isotherms measured at 25 °C and 50°C are also provided.

A lower Si/Al ratio however, can reduce the total pore volume and ultimately the equilibrium capacity (at higher adsorption pressures) of a zeolite due to the steric hinderance of the additional (and potentially much larger, e.g. K) cations in the framework [48]. Modelling of the equilibrium isotherms is critical for proper understanding of the mechanisms and enables effective design of an adsorption system [79–81]. In this work, four individual isotherm models have been assessed for quality of fit (Table 6). The models have been fitted *via* non-linear least squares regression using MATLAB r2023a with the goodness-of-fit estimated through the coefficient of determination (R^2) which has been adjusted for the number of predictors in the model (adj-R^2), and the root mean squared error (RMSE).

Table 6: Adsorption isotherm models assessed in this work.

Model	Equation	Fitting Parameters
Freundlich	$q_e = K_F \cdot P^{1/n_F}$	K_F, n_F

Langmuir	$q_e = \frac{q_{max} \cdot K_L \cdot P}{1 + K_L \cdot P}$	q_{max}, K_L
Sips	$q_e = \frac{q_{max} \cdot K_S \cdot P^{n_S}}{1 + K_s \cdot P^{n_S}}$	q_{max}, K_S, n_s
Toth	$q_e = \frac{q_{max} \cdot P}{(b + P^{n_T})^{\frac{1}{n_T}}}$	$q_{max}, b = \frac{1}{K_T}, n_T$

The Toth equilibrium isotherm model was identified as the best fit for the measured data and the results of the analysis are provided in Table 7. The best fitting model (Toth) is plotted alongside the discrete experimental data in Figure 10. The three model parameters q_{max}, K_T and n_T represent the predicted saturation capacity, the affinity parameter and the Toth constant, respectively. The Toth constant denotes the inhomogeneity of an adsorbent surface and is typically less than 1; when $n_T = 1$, the equation reduces to the Langmuir model demonstrating homogeneity [82]. The Toth constant is temperature dependent and is expected to approach unity as the temperature increases [83]. This can be seen in Table 7 with significant deviation from unity at 0 °C ($n_T = 0.227$) increasing two-fold at 40 °C ($n_T = 0.415$). The heterogeneity of the samples is a result of the presence of multiple phases which can facilitate CO_2 adsorption, in this case type A and type X frameworks alongside amorphous geopolymers each of which can present very different adsorption mechanisms and hence affinities [84]. Even for pure phases, zeolites possess energetically different adsorption sites largely due to the type and distribution/position of framework cations [27]. For both type A and type X zeolites there are multiple possible cation sites which have varying levels of occupation dependant on the Si/Al ratio of the zeolite and both the size and charge of the cations [73]. The reduction in heterogeneity with an increase in temperature could be attributed to an increase in the adsorbate mobility and/or lateral interactions (adsorbate-adsorbate) [85], narrowing the distribution of adsorption site energies [86], as the low energy sites become less viable such as those which rely on contribution from van der Waals dispersion interactions (i.e. Debye, London and Keesom) between CO_2 and the zeolite framework.

Table 7: Results of the non-linear regression with Toth isotherm model fitting.

Temperature, °C	Model Parameters			Adj-R^2	RMSE
	q_{max}	K_T	n_T		
0	5.173	6.930	0.227	0.9977	0.0337
10	3.956	6.840	0.319	0.9986	0.0301
20	3.541	5.963	0.368	0.9992	0.0208
25	3.403	5.488	0.392	0.9995	0.0143
40	3.749	3.409	0.415	0.9994	0.0171

Table 8 presents examples of ash-derived zeolites synthesised using alkaline fusion hydrothermal (AFHT) or hydrothermal (HT) procedures. The CO_2 adsorption capacity of the zeolite produced in this work is well aligned with the capacities of similar sorbents in the literature. Due to the limited number of studies pertaining to industrial-grade biomass combustion ashes, comparison is made to coal fly-ash (CFA) derived zeolites which have a slightly higher adsorption capacity and selectivity. Of the examples in Table 9, only two [87,88] have been produced using a similar methodology (*i.e.* not requiring pretreatment or the addition of extra aluminium). The simple synthesis procedure employed in this work demonstrates a potential pathway for industrially produced biomass ash valorisation.

*Table 8: Ash-derived zeolites in the published literature and their CO_2 adsorption capacities. *Capacity estimated from isotherm plot.*

Precursor	Synthesis Method	Zeolite Type	Degassing Conditions	CO_2 Adsorption Capacity	CO_2/N_2 Selectivity	Ref
Coal Fly Ash	AFHT	X	260 °C Helium	3.21 (0 °C, 1 bar)		[31]
Coal Fly Ash	AFHT	X	300 °C Vacuum	3.25* (50 °C, 1 bar)		[67]
Coal Fly Ash	AFHT	A	300 °C Vacuum	2.47* (50 °C, 1 bar)		[67]
Coal Fly Ash	AFHT	X	260 °C Helium	3.1 (0 °C, 1 bar)	24.2	[87]
Coal Fly Ash	AFHT	X	400 °C Nitrogen	3.03 (0 °C, 1 bar)		[50]
Coal Fly Ash	AFHT	X	450 °C	2.43 (40 °C, 1 bar)		[58]
Coal Fly Ash	AFHT	X	300 °C	3.23* (50 °C, 1 bar)	21.5	[89]
Coal Fly Ash	AFHT	A	300 °C	2.42* (50 °C, atm)	17.3	[89]
Coal Fly Ash (gasification)	AFHT	X	500 °C Argon	3.3 (25 °C, 1 bar)		[88]
Palm Oil Fly Ash	AFHT	X		4.47* (32 °C, 1 bar)		[90]
Rice Husk Ash	HT	X	250 °C Vacuum	4.7 (40 °C, 1 bar)		[91]
Rice Husk Ash	HT	X	350 °C	3.12 (0 °C, 1 bar)	20.3	[92]
Rice Husk Ash	HT	A	350 °C	1.46 (0 °C, 1 bar)	9.7	[92]
Biomass Fly Ash	AFHT	A & X	350 °C N_2	2.92 (0 °C, 1 bar) 2.27 (25 °C, 1 bar)	9.4 14.2	This work

3.4.3. Adsorption Kinetics

The kinetics associated with ZOPT's adsorption of CO_2 has been evaluated by fitting kinetic models to the measured TGA uptake data at 50 °C and 1 bar CO_2. Although not representative of the scale or configuration of the adsorption process, this still provides some insight into the specific mechanisms which underpin, and ultimately limit the rate of adsorption. The data was fitted with 5 individual kinetic models: Pseudo first (PFO) and second order (PSO), Elovich, Weber & Morris Intraparticle diffusion

(IPD) and Avrami models. Both the PFO and PSO fit the data poorly; the other three models together with the fitting results are presented in Table 9.

Table 9: Results of the non-linear kinetic model fitting.

Model	Equation	Model Parameters	R^2	RMSE
Elovich	$q_t = \frac{1}{\beta}\ln(1+\alpha\beta t)$	$\alpha = 190.1$ $\beta = 0.103$	0.943	2.376
W&M Intraparticle Diffusion	$q_t = k_{IPD} \cdot t^{1/2} + C$	$k_{IPD} = 2.62$ $C = 45.55$	0.921	2.795
Avrami	$q_t = q_e\left(1 - e^{(-k_A t)^{n_A}}\right)$	$k_A = 0.09$ $n_A = 0.394$	0.877	3.491

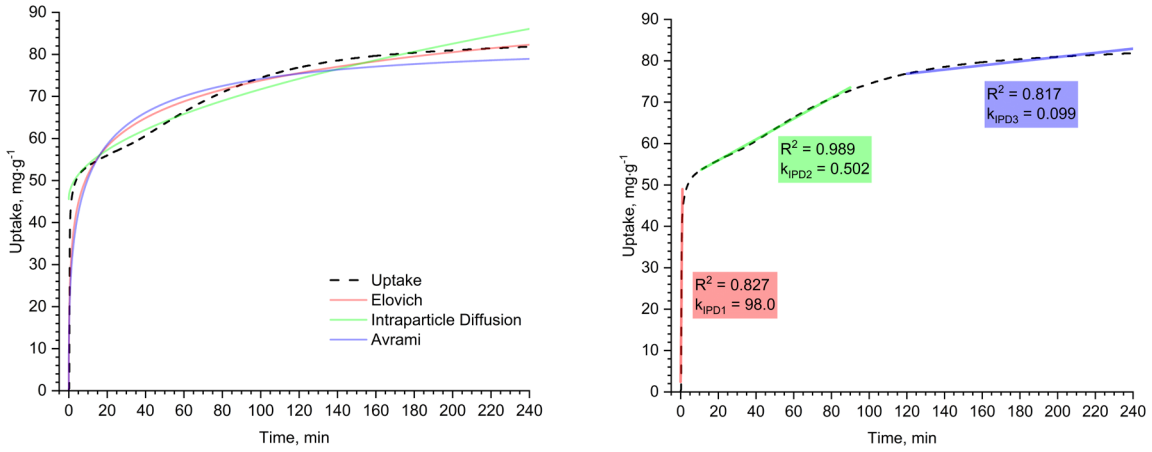

Figure 12: Left - ZOPT CO_2 adsorption kinetic model fitting; Elovich, Avrami and W&M Intraparticle Diffusion model shown. Right - CO_2 adsorption kinetics (ZOPT) at 50 °C and 1 bar fitting with piecewise Intraparticle Diffusion model.

Based on the R^2 and RMSE values, the Elovich model can be seen to best fit the measured data (Figure 12, left). The Elovich model is empirical and lacks a definitive physical meaning of the model parameters [93] however, it is commonly employed to describe heterogeneous systems and/or chemisorption in gas-solid systems [94]. The equation describes the process of adsorption as a collection of reactions which includes diffusion (of the bulk phase, surface diffusion and active catalytic surfaces); it also considers the variation of energetics in relation to surface coverage and the decrease in adsorption rate [95,96], further supporting the hypothesis of ZOPT's heterogeneity. Visually however, all three of the kinetic models fail to accurately describe the three (visually) distinct regions in the measured data. This can be a result of the existence of multiple diffusion mechanisms, determining the rate of adsorption [97]. This was confirmed by plotting q_t *vs* $t^{1/2}$ which revealed the three individual linear regions. The data has therefore, been fitted with a piecewise IPD function which

is theoretically consistent with the original model based on the recommendations of Wang and Guo [98]; the equations are provided in EQ. 2, EQ. 3 and EQ. 4, and the fitted plot in Figure 12 (right).

$$q_t = k_{IPD1} \cdot t^{1/2} \quad \text{EQ. 2}$$

$$q_t - q_{t1} = k_{IPD2}(t - t_1)^{1/2} \quad \text{EQ. 3}$$

$$q_t - q_{t2} = k_{IPD3}(t - t_2)^{1/2} \quad \text{EQ. 4}$$

The IPD model can only represent the mass transfer step which is limited by intraparticle diffusion. It has however, revealed that three main steps exist in the adsorption of CO_2 by ZOPT. It can be seen that the rate constant decreases in the order of $k_{IPD1} < k_{IPD2} < k_{IPD3}$ suggesting a gradual reduction in adsorption rate and an increase in the diffusional resistance [58]. The initial adsorption rate is significant as a result of strong adsorbent-adsorbate interactions [99], lending ZOPT towards application in kinetic separations, within the first minute, the adsorption capacity was recorded at 1.2 $mmolg^{-1}$, 65 % of the measured equilibrium.

3.5. Enthalpy of CO_2 Adsorption

The enthalpy of adsorption can be estimated for a specific adsorptive through analysis of the adsorbent's equilibrium adsorption isotherms. It can be calculated *via* the Clausius-Clapeyron equation which is provided in EQ. 5 where p is the vapor pressure, T is the absolute temperature and ΔH_{ads} is the molar enthalpy of adsorption.

$$\frac{dp}{dT} = \frac{p \cdot \Delta H_{ads}}{-RT^2} \quad \text{EQ. 5}$$

In this research the methodology provided by Nuhnen and Janiak [100] is adopted using the model parameters provided by the Toth isotherm fitting. Knowledge of this property facilitates estimation of the energy requirement for removing the adsorbate from the spent adsorbent. In the context of temperature swing processes this would increase the heat demand for regeneration. The isosteric enthalpy of adsorption for ZOPT has been calculated as -40.2 $kJmol^{-1}$. This value increases at lower loadings, reaching a maximum at around -86 $kJmol^{-1}$ close to zero coverage, further supporting the notion that ZOPT presents significant heterogeneity. This heterogeneity results in the few adsorption sites which have the highest energies being occupied at the lowest coverage [100]. These sites are those provided by the cations within the framework which have been reported to present enthalpies of adsorption between -30 and -90 $kJmol^{-1}$ [27]. The enthalpy of adsorption is expected to drop to a value between -20 to -30 $kJmol^{-1}$ at higher adsorption pressures (> 1 bar). Here, the main adsorbate-adsorbent interactions arise from the interaction of CO_2 with the framework oxygen [101].

3.6. Working capacity

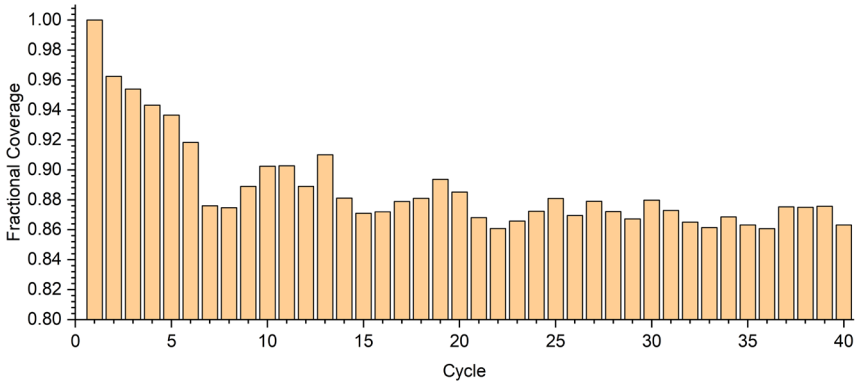

Figure 13: Working CO_2 adsorption capacity of the optimised BFA-derived zeolite. Adsorption at 50 °C, 100 mol%CO_2 at 1 atm for 2 h; desorption at 150 °C, 100 mol%N_2 at 1 atm for 1 h.

Although knowledge of the isosteric enthalpy of adsorption facilitates approximation of the energy demand for adsorbent regeneration, in order to understand the working capacity of ZOPT, a simulated temperature swing adsorption process has been employed. Repetition of an adsorption (50°C, 50 $mLmin^{-1}$ CO_2, 1 atm) and desorption (150°C, 50 $mLmin^{-1}$ N_2, 1 atm) step for a total of 40 complete cycles was carried out *via* TGA. The duration of the adsorption and desorption steps was 2 and 1 h, respectively. The data is presented in Figure 13 where θ is the uptake as a fraction based on the original uptake. There is a strong decline in capacity between cycle 1 and cycle 6 before the value stabilises at a 0.85 with some oscillation for the subsequent cycles. This reduction is quite significant after 40 cycles as most commercial adsorbents are expected to stay in operation for significantly longer. This could be the result of insufficient cycle times for both the adsorption and more importantly the desorption steps which may fail to fully regenerate the adsorbent. Hysteresis is quite commonly reported for type A zeolites which belong to the small-pore classification, where adsorption tends to be limited by the diameter of the α-cages whilst desorption is controlled by the effective pore aperture [102].

4. Conclusion

The hydrothermal conditions of an alkaline fusion-assisted synthesis have been optimised through Taguchi Design of Experiment employing an L9 OA by evaluating the effect of 4 parameters at 3 levels on the prepared adsorbent's equilibrium CO_2 uptake. Both the temperature and duration of the hydrothermal treatment alongside the liquid to solid ratio were observed to be statistically significant with an optimum set of conditions identified with a 90 °C hydrothermal treatment for 10 h employing a liquid to solid ratio of 5. The ratio of NaOH to fly ash was revealed have no statistically significant main effect on the dependent variable or signal to noise ratios. The optimum sample presented an equilibrium CO_2 adsorption capacity of 1.84 $mmolg^{-1}$ measured with 100 mol%CO_2 *via* TGA at 50 °C; volumetric measurements confirmed this capacity which reached a maximum of 2.92 $mmolg^{-1}$ at 0 °C and 1 bar. Modelling of the equilibrium and kinetic isotherms revealed a heterogeneous adsorbent with

various adsorption sites and multiple rate-controlling mechanisms which is to be expected from a mixed-phase zeolite as confirmed by XRD. The enthalpy of adsorption was identified to be coverage dependent with a calculated value at zero coverage of -86 $kJmol^{-1}$ reducing to -40.2 $kJmol^{-1}$ at a coverage of 2 $mmolg^{-1}$. The working capacity of the adsorbent over 40 cycles was measured to be around 85% which was attributed to an insufficient desorption temperature and time. This work presents a feasible route to biomass combustion ash valorisation in the context of carbon capture and storage. The production of high performing zeolites detailed in this paper intends to reveal the potential value in this waste resource as a precursor to value-added adsorbents and catalysts. Future work should focus on scaling up the synthesis of zeolites before assessment of the adsorbent's performance in a representative process configuration to reveal the mass transfer phenomena and breakthrough performance. This will allow assessment of the expected efficiency for biomass-combustion fly ash-derived kinetic separations.

Acknowledgements

This work has been funded by the UK Carbon Capture and Storage Research Centre (EP/W002841/1) through the flexible funded research programme "Investigation of Environmental and Operational Challenges of Adsorbents Synthesised from Industrial Grade Biomass Combustion Residues". The UKCCSRC is supported by the Engineering and Physical Sciences Research Council (EPSRC), UK, as part of the UKRI Energy Programme.

This work has also been supported by the UK's Natural Environment Research Council (NERC), as part of the UKRI, via the NERC Studentship (PhD) Award (project reference: 2360667).

The authors would like to thank and acknowledge the Experimental Techniques Centre (ETC) at Brunel University London and their scientific officers (namely, Dr Ashley Howkins, Dr Myles Worsley, Dr Nicholas Nelson, Dr Uche Onwukwe and Dr Sophia Haghani) for facilitating access to analytical equipment and their continued support.

Last but not least, we would also like to acknowledge the continued generous support from Drax Group UK, with a special thanks to Dr James Hammerton throughout this research.

Author Contributions

BP: Writing (Original Draft & Editing), Conceptualisation, Methodology, Investigation, Formal Analysis, Validation, Visualisation; **MG**: Methodology; Validation; Visualisation; **SMS (corresponding author)**: Supervision, Funding Acquisition, Writing (Review & Editing), Resources, Conceptualisation, Project Administration.

Data Availability Statement

Data have been made available in Brunel University London's repository *via* Brunel Figshare database.

Declaration of Competing Interest

The authors declare that they have no known competing financial interests or personal relationships that could have appeared to influence the work reported in this paper.

5. References

1. BEIS. Net Zero Strategy: Build Back Greener. Gov.Uk. 2021.

2. Almena A, Thornley P, Chong K, Röder M. Carbon dioxide removal potential from decentralised bioenergy with carbon capture and storage (BECCS) and the relevance of operational choices. Biomass and Bioenergy. 2022;159.

3. Friedlingstein P, O'Sullivan M, Jones MW, Andrew RM, Gregor L, Hauck J, et al. CO_2 and Greenhouse Gas Emissions. Our World Data. 2020;14(11).

4. IPCC. SYNTHESIS REPORT OF THE IPCC SIXTH ASSESSMENT REPORT (AR6): Summary for Policymakers. European University Institute. 2023.

5. McQueen N, Gomes KV, McCormick C, Blumanthal K, Pisciotta M, Wilcox J. A review of direct air capture (DAC): Scaling up commercial technologies and innovating for the future. Vol. 3, Progress in Energy. 2021.

6. Rosa L, Sanchez DL, Mazzotti M. Assessment of carbon dioxide removal potential: Via BECCS in a carbon-neutral Europe. Energy Environ Sci. 2021;14(5).

7. Climate Change Committee. The Sixth Carbon Budget: The UK's path to Net Zero. Carbon Budg. 2020;(December).

8. García-Freites S, Gough C, Röder M. The greenhouse gas removal potential of bioenergy with carbon capture and storage (BECCS) to support the UK's net-zero emission target. Biomass and Bioenergy. 2021;151.

9. BEIS. UK ENERGY IN BRIEF 2022. Gov.UK. 2022.

10. Department for Energy Security and Net Zero. Biomass Strategy 2023. London; 2023.

11. Drax. Drax sets world-first ambition to become carbon negative by 2030. 2019.

12. Belviso C. State-of-the-art applications of fly ash from coal and biomass: A focus on zeolite synthesis processes and issues. Prog Energy Combust Sci [Internet]. 2018;65:109–35. Available from: https://doi.org/10.1016/j.pecs.2017.10.004

13. Zając G, Szyszlak-Bargłowicz J, Gołębiowski W, Szczepanik M. Chemical characteristics of biomass ashes. Energies. 2018;11(11):1–15.

14. Ahmaruzzaman M. A review on the utilization of fly ash. Prog Energy Combust Sci. 2010;36(3):327–63.

15. Vassilev S V., Vassileva CG. Extra CO_2 capture and storage by carbonation of biomass ashes. Energy Convers Manag [Internet]. 2020;204(November):112331. Available from: https://doi.org/10.1016/j.enconman.2019.112331

16. Gorbounov M, Petrovic B, Ozmen S, Clough P, Masoudi Soltani S. Activated carbon derived from Biomass combustion bottom ash as solid sorbent for CO_2 adsorption. Chem Eng Res Des. 2023;194.

17. Williams A. Understanding slagging and fouling during PF combustion Gordon Couch IEA Coal Research, London, 1994, pp. 109, ISBN 92-9029-240-7, £85. Fuel. 1995;74(10).

18. Kleinhans U, Wieland C, Frandsen FJ, Spliethoff H. Ash formation and deposition in coal and biomass fired combustion systems: Progress and challenges in the field of ash particle sticking and rebound behavior. Vol. 68, Progress in Energy and Combustion Science. 2018.

19. Wu H, Wall T, Liu G, Bryant G. Ash liberation from included minerals during combustion of pulverized coal: The relationship with char structure and burnout. Energy and Fuels. 1999;13(6).

20. Bae YS, Snurr RQ. Development and evaluation of porous materials for carbon dioxide separation and capture. Angew Chemie - Int Ed. 2011;50(49):11586–96.

21. Aaron D, Tsouris C. Separation of CO_2 from flue gas: A review. In: Separation Science and Technology. 2005.

22. Choi S, Drese JH, Jones CW. Adsorbent materials for carbon dioxide capture from large anthropogenic point sources. ChemSusChem. 2009;2(9):796–854.

23. Petrovic B, Gorbounov M, Masoudi Soltani S. Impact of Surface Functional Groups and Their Introduction Methods on the Mechanisms of CO_2 Adsorption on Porous Carbonaceous Adsorbents. Vol. 3, Carbon Capture Science and Technology. 2022.

24. Saha D, Kienbaum MJ. Role of oxygen, nitrogen and sulfur functionalities on the surface of nanoporous carbons in CO_2 adsorption: A critical review. Microporous Mesoporous Mater [Internet]. 2019;287(April):29–55. Available from: https://doi.org/10.1016/j.micromeso.2019.05.051

25. Millward AR, Yaghi OM. Metal-organic frameworks with exceptionally high capacity for storage of carbon dioxide at room temperature. J Am Chem Soc. 2005;127(51).

26. Ding M, Flaig RW, Jiang HL, Yaghi OM. Carbon capture and conversion using metal-organic frameworks and MOF-based materials. Chem Soc Rev. 2019;48(10):2783–828.

27. Boer DG, Langerak J, Pescarmona PP. Zeolites as Selective Adsorbents for CO_2 Separation. ACS Appl Energy Mater. 2023;6(5):2634–56.

28. Cundy CS, Cox PA. The hydrothermal synthesis of zeolites: Precursors, intermediates and reaction mechanism. Microporous Mesoporous Mater. 2005;82(1–2):1–78.

29. Samanta NS, Das PP, Mondal P, Changmai M, Purkait MK. Critical review on the synthesis and advancement of industrial and biomass waste-based zeolites and their applications in gas adsorption and biomedical studies. J Indian Chem Soc. 2022;99(11).

30. Petrovic B, Gorbounov M, Ozmen S, Clough P, Soltani SM. Synthesis of Nanoporous Type A and X Zeolite Mixtures from Biomass Combustion Fly Ash for Post-Combustion Carbon Capture. In: Proceedings of the IEEE Conference on Nanotechnology. 2022.

31. Boycheva S, Zgureva D, Lazarova H, Popova M. Comparative Studies of Carbon Capture onto Coal Fly Ash Zeolites Na-X and Na-Ca-X. Chemosphere [Internet]. 2021;271:129505. Available from: https://doi.org/10.1016/j.chemosphere.2020.129505

32. Vassilev S V., Vassileva CG. Methods for characterization of composition of fly ashes from coal-fired power stations: A critical overview. Vol. 19, Energy and Fuels. 2005.

33. Collins F, Rozhkovskaya A, Outram JG, Millar GJ. A critical review of waste resources, synthesis, and applications for Zeolite LTA. Microporous Mesoporous Mater [Internet]. 2020;291(August 2019):109667. Available from: https://doi.org/10.1016/j.micromeso.2019.109667

34. Khaleque A, Alam MM, Hoque M, Mondal S, Haider J Bin, Xu B, et al. Zeolite synthesis from low-cost materials and environmental applications: A review. Vol. 2, Environmental Advances. 2020.

35. El-Naggar MR, El-Kamash AM, El-Dessouky MI, Ghonaim AK. Two-step method for preparation of NaA-X zeolite blend from fly ash for removal of cesium ions. J Hazard Mater. 2008;154(1–3):963–72.

36. Bukhari SS, Behin J, Kazemian H, Rohani S. Conversion of coal fly ash to zeolite utilizing microwave and ultrasound energies: A review. Fuel. 2015;140:250–66.

37. Petrovic B, Gorbounov M, Lahiri A, Masoudi Soltani S. Biomass Combustion Fly Ash-Derived Nanoporous Zeolites for Post-Combustion Carbon Capture; Biomass Combustion Fly Ash-Derived Nanoporous Zeolites for Post-Combustion Carbon Capture. 2021; Available from: https://ec.europa.eu/clima/policies/international/negotiations/pa

38. Gorbounov M, Taylor J, Petrovic B, Masoudi Soltani S. To DoE or not to DoE? A Technical Review on & Roadmap for Optimisation of Carbonaceous Adsorbents and Adsorption Processes. Vol. 41, South African Journal of Chemical Engineering. 2022.

39. Petrovic BA, Soltani SM. Optimization of post combustion CO_2 capture from a combined-cycle gas turbine power plant via taguchi design of experiment. Processes. 2019;7(6).

40. Brunauer S, Emmett PH, Teller E. Adsorption of Gases in Multimolecular Layers. J Am Chem Soc. 1938;60(2).

41. Das SK, Sahoo P. Wear performance optimization of electroless Ni-B coating using Taguchi design of experiments. Tribol Ind. 2010;32(4).

42. Gorbounov M, Diaz-Vasseur E, Danaci D, Masoudi Soltani S. Chemical activation of porous carbon extracted from biomass combustion bottom ash for CO_2 adsorption. Carbon Capture Sci Technol. 2024 Mar 1;10:100151.

43. Anbia M, Nejati FM, Jahangiri M, Eskandari A, Garshasbi V. Optimization of synthesis procedure for NaX zeolite by taguchi experimental design and its application in CO_2 adsorption. J Sci Islam Repub Iran. 2015;26(3):213–22.

44. Mainganye D, Ojumu TV, Petrik L. Synthesis of zeolites Na-P1 from South African coal fly ash: Effect of impeller design and agitation. Materials (Basel). 2013;

45. Vassilev S V., Baxter D, Vassileva CG. An overview of the behaviour of biomass during combustion: Part II. Ash fusion and ash formation mechanisms of biomass types. Fuel [Internet]. 2014;117(PART A):152–83. Available from: http://dx.doi.org/10.1016/j.fuel.2013.09.024

46. Benson SA, Hurley JP, Zygarlicke CJ, Steadman EN, Erickson TA. Predicting Ash Behavior in Utility Boilers. Energy and Fuels. 1993;7(6).

47. Srinivasachar S, Boni AA. A kinetic model for pyrite transformations in a combustion environment. Fuel. 1989 Jul 1;68(7):829–36.

48. Cornelius MLU, Price L, Wells SA, Petrik LF, Sartbaeva A. The steric influence of extra-framework cations on framework flexibility: An LTA case study. Zeitschrift fur Krist - Cryst Mater. 2019;234(7–8):461–8.

49. Ren X, Qu R, Liu S, Zhao H, Wu W, Song H, et al. Synthesis of zeolites from coal fly ash for the removal of harmful gaseous pollutants: A review. Aerosol Air Qual Res. 2020;20(5):1127–44.

50. Popova M, Boycheva S, Lazarova H, Zgureva D, Lázár K, Szegedi Á. VOC oxidation and CO_2 adsorption on dual adsorption/catalytic system based on fly ash zeolites. Catal Today [Internet]. 2020;357(June 2019):518–25. Available from: https://doi.org/10.1016/j.cattod.2019.06.070

51. Molina A, Poole C. A comparative study using two methods to produce zeolites from fly ash. Miner Eng. 2004;17(2):167–73.

52. Klunk MA, Das M, Dasgupta S, Impiombato AN, Caetano NR, Wander PR, et al. Comparative study using different external sources of aluminum on the zeolites synthesis from rice husk ash. Mater Res Express. 2019;7(1).

53. Panek R, Madej J, Bandura L, Słowik G. Recycling of waste solution after hydrothermal conversion of fly ash on a semi-technical scale for Zeolite synthesis. Materials (Basel). 2021;14(6):1–16.

54. Babajide O, Musyoka N, Petrik L, Ameer F. Novel zeolite Na-X synthesized from fly ash as a heterogeneous catalyst in biodiesel production. Catal Today. 2012;190(1).

55. Sing K. The use of nitrogen adsorption for the characterisation of porous materials. In: Colloids and Surfaces A: Physicochemical and Engineering Aspects. 2001.

56. Hong JLX, Maneerung T, Koh SN, Kawi S, Wang CH. Conversion of Coal Fly Ash into Zeolite Materials: Synthesis and Characterizations, Process Design, and Its Cost-Benefit Analysis. Ind Eng Chem Res. 2017;56(40):11565–74.

57. Thommes M, Kaneko K, Neimark A V., Olivier JP, Rodriguez-Reinoso F, Rouquerol J, et al. Physisorption of gases, with special reference to the evaluation of surface area and pore size distribution (IUPAC Technical Report). Pure Appl Chem. 2015;87(9–10):1051–69.

58. Guo J, Wu H, Wei Y, Miao Y, Qu J, Wang P. Synthesis of a high-iron fly-ash-based Na-X molecular sieve and its application in the adsorption of low concentration of CO_2. RSC Adv. 2024;14(3):1686–96.

59. Boycheva S, Zgureva D, Lazarova K, Babeva T, Popov C, Lazarova H, et al. Progress in the Utilization of Coal Fly Ash by Conversion to Zeolites with Green Energy Applications. Materials (Basel). 2020;13(9):2014.

60. Bukhari SS, Behin J, Kazemian H, Rohani S. A comparative study using direct hydrothermal and indirect fusion methods to produce zeolites from coal fly ash utilizing single-mode microwave energy. J Mater Sci. 2014;49(24):8261–71.

61. Hartmann M, Thommes M, Schwieger W. Hierarchically-Ordered Zeolites: A Critical Assessment. Adv Mater Interfaces. 2021;8(4).

62. Rouquerol J, Llewellyn P, Rouquerol F. Is the BET equation applicable to microporous adsorbents? Stud Surf Sci Catal. 2007;160.

63. Dantas S, Struckhoff KC, Thommes M, Neimark A V. Pore size characterization of micro-mesoporous carbons using CO_2 adsorption. Carbon N Y. 2021;173.

64. Terrones GG, Chen Y, Datar A, Lin L-C, Kulik HJ, Chung YG. SESAMI APP: An Accessible Interface for Surface Area Calculation of Materials from Adsorption Isotherms. J Open Source Softw [Internet]. 2023 Jun 9;8(86):5429. Available from: https://doi.org/10.21105/joss.05429

65. Lopes A, Moura-nickel CD, Scaratti G, Rossi A De, Helena M, Noni A De, et al. Geopolymers produced with fl y ash and rice husk ash applied to **CO_2** capture. 2020;273.

66. de Aquino TF, Estevam ST, Viola VO, Marques CRMM, Zancan FL, Vasconcelos LB, et al. CO_2 adsorption capacity of zeolites synthesized from coal fly ashes. Fuel [Internet]. 2020;276(May):118143. Available from: https://doi.org/10.1016/j.fuel.2020.118143

67. Verrecchia G, Cafiero L, de Caprariis B, Dell'Era A, Pettiti I, Tuffi R, et al. Study of the parameters of zeolites synthesis from coal fly ash in order to optimize their CO_2 adsorption. Fuel [Internet]. 2020;276(March):118041. Available from: https://doi.org/10.1016/j.fuel.2020.118041

68. Liu J, Wei J. Knudsen diffusion in channels and networks. Chem Eng Sci. 2014 May 24;111:1–14.

69. Grande CA. Advances in Pressure Swing Adsorption for Gas Separation. ISRN Chem Eng. 2012;2012.

70. Cheung O, Wardecki D, Bacsik Z, Vasiliev P, McCusker LB, Hedin N. Highly selective uptake of carbon dioxide on the zeolite |na10.2KCs0.8|- LTA -a possible sorbent for biogas upgrading. Phys Chem Chem Phys. 2016;18(24).

71. Yeh YT, Yang RT. Diffusion in zeolites containing mixed cations. AIChE J. 1989;35(10).

72. García-Sánchez A, García-Pérez E, Dubbeldam D, Krishna R, Calerọ S. A simulation study of alkanes in Linde Type A zeolites. Adsorpt Sci Technol. 2007;25(6).

73. Kulprathipanja S. Zeolites in Industrial Separation and Catalysis. Zeolites in Industrial Separation and Catalysis. 2010.

74. Sarker AI, Aroonwilas A, Veawab A. Equilibrium and Kinetic Behaviour of CO_2 Adsorption onto Zeolites, Carbon Molecular Sieve and Activated Carbons. In: Energy Procedia. 2017. p. 2450–9.

75. Yu Q, Cai Y, Zhang Q, Li Y, Sun N, Liu W, et al. Silica-alumina zeolite adsorbents for oxygen generation via pressure swing adsorption: Mechanisms and challenge. Chem Eng J. 2024 Feb 1;481:148788.

76. Cheung O, Hedin N. Zeolites and related sorbents with narrow pores for CO_2 separation from flue gas. Vol. 4, RSC Advances. 2014. p. 14480–94.

77. Shen M, Kong F, Guo W, Zuo Z, Gao T, Chen S, et al. Impact of H_2O on CO_2 adsorption and co-adsorption: Mechanism and high-performance adsorbents for efficient H_2O - CO_2 capture. Chem Eng J. 2024 Jan 1;479:147923.

78. Zhao J, Deng S, Zhao L, Yuan X, Wang B, Chen L, et al. Synergistic and competitive effect of H_2O on CO_2 adsorption capture: Mechanism explanations based on molecular dynamic simulation. J CO_2 Util [Internet]. 2021;52(January):101662. Available from: https://doi.org/10.1016/j.jcou.2021.101662

79. El-Khaiary MI. Least-squares regression of adsorption equilibrium data: Comparing the options. J Hazard Mater. 2008 Oct 1;158(1):73–87.

80. Ayawei N, Ebelegi AN, Wankasi D. Modelling and Interpretation of Adsorption Isotherms. J Chem. 2017;2017.

81. Taylor JH, Masoudi Soltani S. Carbonaceous adsorbents in the removal of aquaculture pollutants: A technical review of methods and mechanisms. Ecotoxicol Environ Saf. 2023 Nov 1;266:115552.

82. Mozaffari Majd M, Kordzadeh-Kermani V, Ghalandari V, Askari A, Sillanpää M. Adsorption isotherm models: A comprehensive and systematic review (2010−2020). Sci Total Environ. 2022;812(xxxx).

83. Son KN, Cmarik GE, Knox JC, Weibel JA, Garimella S V. Measurement and Prediction of the Heat of Adsorption and Equilibrium Concentration of CO_2 on Zeolite 13X. J Chem Eng Data. 2018;63(5):1663–74.

84. Candamano S, Policicchio A, Conte G, Abarca R, Algieri C, Chakraborty S, et al. Preparation of foamed and unfoamed geopolymer/NaX zeolite/activated carbon composites for CO_2 adsorption. J Clean Prod. 2022 Jan 1;330:129843.

85. Bonenfant D, Kharoune M, Niquette P, Mimeault M, Hausler R. Advances in principal factors influencing carbon dioxide adsorption on zeolites. Sci Technol Adv Mater. 2008;9(1).

86. Kumar KV, Gadipelli S, Howard CA, Kwapinski W, Brett DJL. Probing adsorbent heterogeneity using Toth isotherms. J Mater Chem A. 2021;9(2):944–62.

87. Zgureva D, Boycheva S. Experimental and model investigations of CO_2 adsorption onto fly ash zeolite surface in dynamic conditions. Sustain Chem Pharm [Internet]. 2020;15(January):100222. Available from: https://doi.org/10.1016/j.scp.2020.100222

88. Verrecchia G, Cafiero L, de Caprariis B, Dell'Era A, Pettiti I, Tuffi R, et al. Study of the parameters of zeolites synthesis from coal fly ash in order to optimize their CO_2 adsorption. Fuel [Internet]. 2020;276(January):118041. Available from: https://doi.org/10.1016/j.fuel.2020.118041

89. Morales R, Yan O, Eurico GA, Enrique BT, García V, Bastos M, et al. Assessment of the potential use of zeolites synthesized from power plant fly ash to capture - CO_2 under post - combustion

scenario. Adsorption [Internet]. 2020;(0123456789). Available from: https://doi.org/10.1007/s10450-020-00245-0

90. Kongnoo A, Tontisirin S, Worathanakul P, Phalakornkule C. Surface characteristics and CO2adsorption capacities of acid-activated zeolite 13X prepared from palm oil mill fly ash. Fuel [Internet]. 2017;193:385–94. Available from: http://dx.doi.org/10.1016/j.fuel.2016.12.087

91. Gargiulo N, Shibata K, Peluso A, Aprea P, Valente T, Pezzotti G, et al. Reinventing rice husk ash: derived NaX zeolite as a high-performing CO_2 adsorbent. Int J Environ Sci Technol. 2018;15(7):1543–50.

92. Wang Y, Du T, Jia H, Qiu Z, Song Y. Synthesis, characterization and CO_2 adsorption of NaA, NaX and NaZSM-5 from rice husk ash. Solid State Sci [Internet]. 2018;86(September):24–33. Available from: https://doi.org/10.1016/j.solidstatesciences.2018.10.003

93. Wang J, Guo X. Adsorption kinetic models: Physical meanings, applications, and solving methods. J Hazard Mater [Internet]. 2020;390(January):122156. Available from: https://doi.org/10.1016/j.jhazmat.2020.122156

94. Ebelegi AN, Ayawei N, Wankasi D. Interpretation of Adsorption Thermodynamics and Kinetics. Open J Phys Chem. 2020;10(03):166–82.

95. Dąbrowski A. Adsorption - From theory to practice. Vol. 93, Advances in Colloid and Interface Science. 2001.

96. Aharoni C, Tompkins FC. Kinetics of Adsorption and Desorption and the Elovich Equation. Adv Catal. 1970;21(C).

97. Loganathan S, Tikmani M, Edubilli S, Mishra A, Ghoshal AK. CO_2 adsorption kinetics on mesoporous silica under wide range of pressure and temperature. Chem Eng J. 2014;256.

98. Wang J, Guo X. Rethinking of the intraparticle diffusion adsorption kinetics model: Interpretation, solving methods and applications. Chemosphere [Internet]. 2022;309(P2):136732. Available from: https://doi.org/10.1016/j.chemosphere.2022.136732

99. Najafi AM, Soltanali S, Ghassabzadeh H. Enhancing the CO2, CH4, and N2 adsorption and kinetic performance on FAU zeolites for CO_2 capture from flue gas by metal incorporation technique. Chem Eng J. 2023;468(March).

100. Nuhnen A, Janiak C. A practical guide to calculate the isosteric heat/enthalpy of adsorption: Via adsorption isotherms in metal-organic frameworks, MOFs. Dalt Trans. 2020;49(30):10295–307.

101. Grajciar L, Čejka J, Zukal A, Otero Areán C, Turnes Palomino G, Nachtigall P. Controlling the adsorption enthalpy of CO_2 in zeolites by framework topology and composition. ChemSusChem. 2012;5(10):2011–22.

102. De Oliveira LH, Pereira M V., Meneguin JG, De Barros MASD, Do Nascimento JF, Arroyo PA, et al. Influence of regeneration conditions on cyclic CO2adsorption on NaA zeolite at high pressures. Energy and Fuels. 2023;67(April 2022):6641–9.

103. Baerlocher C, McCUsker LB, Hanson RM. Database of Zeolite Structures. www.iza-structure.org/databases/. 2017.